ACS APPLIED MATERIALS & INTERFACES

Research Article

www.acsami.org

Preparation and Enhanced Photocatalytic Activity of TiO_2 Nanocrystals with Internal Pores

Lu Ren,[†] Yuanzhi Li,*[,†] Jingtao Hou,[†] Xiujian Zhao,[†] and Chunxu Pan[‡]

[†]State Key Laboratory of Silicate Materials for Architectures, Wuhan University of Technology, 122 Luoshi Road, Wuhan 430070, P.R. China

[‡]Department of Physics, Wuhan University, Luojia Hill, Wuhan 430072, P.R. China

Supporting Information

ABSTRACT: Anatase TiO_2 nanocrystals with internal pores are prepared by a novel facile microwave-assisted hydrolysis of a mixture of $TiOCl_2$ and HF aqueous solutions, followed by calcination at 400 °C. The TiO_2 nanocrystals with internal pores are characterized by XRD, TEM, SEM, BET, EDS, and XPS. The formation mechanism of the TiO_2 nanocrystals with internal pores is discussed by investigating the role of fluorine and the calcination. The photocatalytic measurement shows that the TiO_2 nanocrystals with internal pores exhibit much higher photocatalytic activity for the photodegradation of crystal violet, methyl orange, and 4-chlorophenol than the TiO_2 solid nanocrystals. The photocatalytic enhancement is due to the fluorination of TiO_2 nanocrystals as well as its unique hollow nanostructure, which results in the higher separation efficiency of photogenerated electrons and holes in the TiO_2 nanocrystals with internal pores than in its solid counterpart.

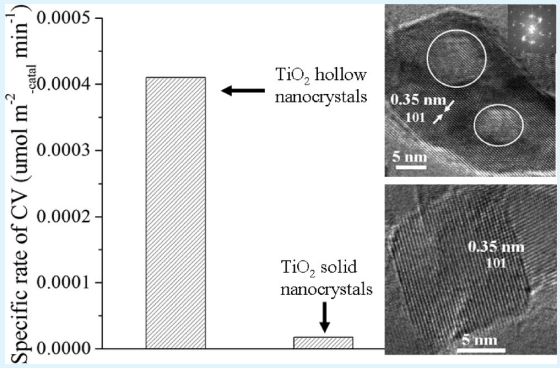

KEYWORDS: *TiO_2, nanocrystals with internal pores, photocatalytic*

1. INTRODUCTION

TiO_2 as a very important semiconductor has been extensively investigated for a vast range of applications such as photocatalytic environmental purification, photocatalytic water splitting for clean H_2 energy, solar cells, antimicrobial activity, self-cleaning, lithium ion batteries, and more, due to its peculiar chemical and physical properties.[1] The photocatalytic performance of TiO_2 is greatly affected by its morphology and structures. Various kinds of nano/microstructured TiO_2, such as nanoparticle, nanocrystal with controllable exposed facets (e.g., {001}), nanorod, nanotube, hollow sphere/nanobox, and mesoporous and macro-/mesoporous TiO_2 have been synthesized and used in the applications.[1−26] As a unique micro/nanostructure, TiO_2 hollow structures have recently attracted a great deal of attention due to their specific features such as low density, high surface-to-volume ratio, and the effect of void space (e.g., light scattering).[2−25] They have exhibited attractive properties for sensors,[2] lithium-ion batteries,[3] solar cells,[4−7] and photocatalysts[8−10] as compared to their solid counterparts. Various strategies have been developed to prepare TiO_2 hollow micro/nanostructures. These strategies include conventional templating synthesis using a variety of hard templates,[11−14] soft templating synthesis using microemulsion droplets, ionic liquids and gas bubbles as templates,[15−17] template-free methods mostly through Ostwald ripening.[10,18−24] and pulsed laser heating process through a mechanism analogous to the Kirkendall effect.[7] Most TiO_2 hollow structures reported are composed of polycrystalline walls of randomly aggregated nanoparticles, and the hollow structure diameters are in the range of microscale. Few works have been reported on the synthesis of single crystalline TiO_2 hollow nanoparticles.

Yin et al. demonstrated the first preparation of hollow CoO nanoparticles through the oxidation of Co NPs, using the concept of the nanoscale Kirkendall effect,[27] which involves two distinct processes such as surface oxidation and vacancy coalescence induced by outward diffusion of the metal atoms. Since then, many hollow and core/shell nanocrystals of oxides and chalcogenides have been synthesized this way.[28−31] However, up to now, TiO_2 hollow nanocrystals with internal pores, which may exhibit unique properties, have not been experimentally realized. The difficulty is due to the easy collapse of porous titania wall in the process of TiO_2 crystallization especially at higher temperature.[32] Therefore, it is challenging and of scientific significance to explore the possibility of the formation of TiO_2 hollow nanocrystals. For the first time, we developed a novel strategy conceptually different from the Kirkendall effect to prepare TiO_2 nanocrystals with internal pores in the presence of fluorine. Interestingly, the TiO_2 nanocrystals with internal pores exhibit enhanced photocatalytic activity as compared to its counterpart of TiO_2 solid nanocrystals due to its unique hollow nanostructure.

Received: October 9, 2013
Accepted: January 1, 2014
Published: January 1, 2014

2. EXPERIMENTAL METHODS

2.1. Preparation. TiO_2 nanocrystals with internal pores were prepared according to the following procedure. Aqueous solution of 0.3 mol L^{-1} $TiOCl_2$ was obtained by dropping known amounts of $TiCl_4$ into 100 mL portions of distilled water in an ice−water bath. Volumes of 75 mL of 0.3 mol L^{-1} $TiOCl_2$ aqueous solution and 6.0 mL of 0.94 mol L^{-1} HF aqueous solution were mixed in a flask. ***Caution!*** *Hydrofluoric acid is extremely corrosive and a contact poison, and it should be handled with extreme care.* The flask was placed in a microwave oven (2450 MHz, 800 W, WBFY-201, Gongyi City Yuhua Instrument Co., Ltd.). Then, the microwave oven was turned on, and the aqueous solution of $TiOCl_2$ and HF was heated for 30 min. The precipitate was filtered, washed thoroughly by distilled water, dried under an infrared lamp, and finally calcined at 400 °C for 2 h in a muffle furnace.

The preparation procedure of TiO_2 solid nanoparticles was similar to that of the above TiO_2 nanocrystals with internal pores but without adding HF. A volume of 75 mL of 0.3 mol L^{-1} $TiOCl_2$ aqueous solution was added in a flask. The flask was placed in a microwave oven. Then, the microwave oven was turned on, and the aqueous solution of $TiOCl_2$ was heated for 30 min. The precipitate was filtered, washed thoroughly by distilled water, dried under an infrared lamp, and finally calcined at 400 °C for 2 h in a muffle furnace.

TiO_2 solid nanocrystals were prepared by a method of vapor induced thermal hydrolysis. The detailed procedure is as follows. Ten milliliters of titanium butoxide (TBOT) in a 20 mL glass bottle was placed into a 100 mL Teflon liner, which was then placed into a stainless steel autoclave. In the gap between the Teflon liner and glass bottle, 20 mL of distilled water was added. The autoclave was placed in an electrical oven, and heated to 180 °C and kept at the temperature for 16 h. After the autoclave was cooled to room temperature, the resulting precipitates were washed with ethanol and then with distilled water, and dried at 120 °C for 10 h. The obtained brown TiO_2 powder was mixed with distilled water, ground to a slurry with an agate mortar. The slurry was coated on a 125 W high pressure Hg lamp, and dried under an infrared lamp. The Hg lamp was turned on for 12 h to efficiently remove the adsorbed organic compounds on the TiO_2 sample by photocatalysis.

The sample of fluorinated TiO_2 solid nanocrystals was prepared according to the following procedure: 0.1184 g of 40.0 wt % HF solution was added to 20.0 mL of distilled water in a Teflon beaker, and then 2.000 g of the TiO_2 solid nanocrystal sample was added to the HF aqueous solution under magnetic stirring. After the stirring for 1 h, the suspension was added to a Teflon dish and dried under an infrared lamp.

2.2. Characterization. X-ray diffraction (XRD) patterns were obtained on a Rigaku Dmax X-ray diffractometer using Cu Kα radiation. Transmission electron microscopy (TEM) images were obtained by using a JEM-100CX electron microscope. The BET surface area was measured on AUTOSDRB-1 using N_2 adsorption at −196 °C for the TiO_2 sample predegassed at 120 °C in vacuum for 2 h. Scanning electron microscopy (SEM) and energy dispersive spectral (EDS) analysis were performed by using a Hitachi S-4800 scanning electron microscope. The samples were analyzed by a VG Multilab 2000 X-ray photoelectron spectrometer (XPS) using Mg Kα radiation. The XPS spectra of the samples were calibrated by referencing the binding energy to adventitious carbon (C 1s, 284.6 eV).

2.3. Photocurrent. Photocurrent measurements were carried out as follows. The TiO_2 powder was mixed with distilled water, ultrasonicated for 2 h, and then ground to slurry with an agate mortar. The TiO_2 slurry was uniformly spread on an ITO glass substrate (1 cm × 1.2 cm). Another ITO glass substrate was covered on the slurry to form an ITO/TiO_2 film/ITO stack. The stack was dried at 120 °C for 12 h in an electrical oven, and then was irradiated for 12 h under a 125 W self-rectified high pressure Hg lamp (Shanghai Yaming Lighting Appliance Co., denoted as UV lamp). The electrical lead of Cu fine wire (Ø 0.1 mm) was attached to the ITO electrodes by using Ag paste. The transient response of photocurrent for the TiO_2 stacks in air was recorded under an operation voltage of 0.5 V on an electrochemical analyzer (CHI750). A 125 W self-rectified high pressure Hg lamp was used as a light source.

2.4. Photocatalytic Activity. The photocatalytic activity of the photocatalysts was evaluated by the photodegradation of crystal violet (CV), methyl orange (MO), and 4-chlorophenol (4-CP). The light source was a 125 W self-rectified high pressure Hg lamp. The reaction was maintained at ambient temperature. In a typical experiment, aqueous suspensions of dye (50 mL, 2.5×10^{-5} mol L^{-1} for CV and MO, 1.0×10^{-4} mol L^{-1} for 4-CP) and 0.2000 g of the photocatalyst powder were placed in the beaker. Prior to irradiation, the suspension was magnetically stirred in the dark to ensure the establishment of an adsorption/desorption equilibrium. The suspension was kept under constant air-equilibrated conditions. At the intervals of given irradiation time, 1 mL of the suspension was collected and centrifuged to remove the particles. The dye concentration was determined by measuring the UV−vis absorbance of the dye aqueous solution.

3. RESULTS AND DISCUSSION

3.1. Preparation and Characterization. TiO_2 nanocrystals with internal pores were prepared by a facile microwave-assisted hydrolysis of a mixture of 75 mL of 0.3 mol/L $TiOCl_2$ aqueous solution and 6 mL of 0.94 mol/L HF aqueous solutions, followed by calcination at 400 °C for 2 h (see Experimental Methods). XRD analysis (Figure 1a) reveals that

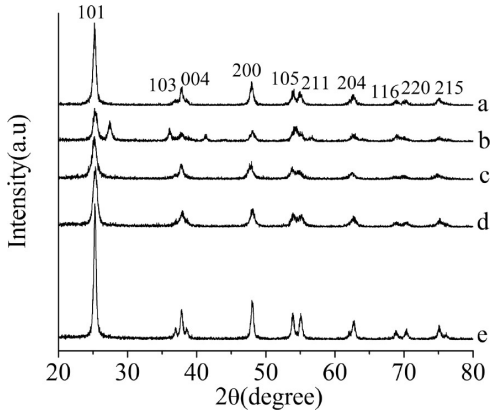

Figure 1. XRD pattern of the TiO_2 samples: (a) the TiO_2 nanocrystals with internal pores, (b) the TiO_2 nanoparticle prepared by the hydrolysis of $TiOCl_2$ in the absence of HF, (c) the uncalcined TiO_2 sample prepared by the hydrolysis of a mixture of $TiOCl_2$ and HF solution but without calcinations at 400 °C, (d) the TiO_2 solid nanocrystals, and (e) the TiO_2 nanocrystals obtained by the calcination at 600 °C for 2 h of the uncalcined TiO_2 sample.

the obtained TiO_2 sample is indexed to the pure anatase structures (JCPDS 89-4921). Its average crystal size, which was determined by the Scherrer formula ($L = 0.89\lambda/\beta \cos \theta$), is 18.8 nm (Table 1). TEM image (Figure 2a) reveals that there is one or more mesopores existed in each of TiO_2 particles with a size range of 6.6−38.7 nm. The hollow structure is clearly visible with a dark-field image as shown in Figure 2b. HRTEM image of a selected TiO_2 nanoparticle together with its corresponding Fourier transforms depict the hollow single crystalline nature of the TiO_2 nanoparticle with two pores (Figure 2c). But no pores in nanoparticles are observed by SEM image (Figure 2d), suggesting that the pores observed by TEM are inside the nanoparticles, not on the surface. The pore size distribution of the TiO_2 nanocrystals with internal pores reveals that their dominant size is 5−7 nm (Figure 2e). The N_2 adsorption−desorption isotherm of the TiO_2 nanocrystal sample with internal pores shows that it presents a desorption

Table 1. Properties of the TiO_2 Samples Prepared under Different Conditions

sample	preparation method	calcination temperature (°C)	morphology	phase	crystallite size (nm)	BET surface area (m^2/g)
a	hydrolysis of $TiOCl_2$ and HF	400	nanocrystals with internal pores	anatase	18.8	73.7
b	hydrolysis of $TiOCl_2$	400	solid nanoparticle	anatase, rutile	13.7(A), 17.1(R)	78.5
c	hydrolysis of $TiOCl_2$ and HF	no	nanoparticles with mesopores	anatase	11.8	190.8
d	hydrothermal hydrolysis of $Ti(OBu)_4$	no	solid nanocrystals	anatase	13.4	120.0
e	hydrolysis of $TiOCl_2$ and HF	600	nanocrystals with internal pores, solid nanocrystals	anatase	25.4	50.1

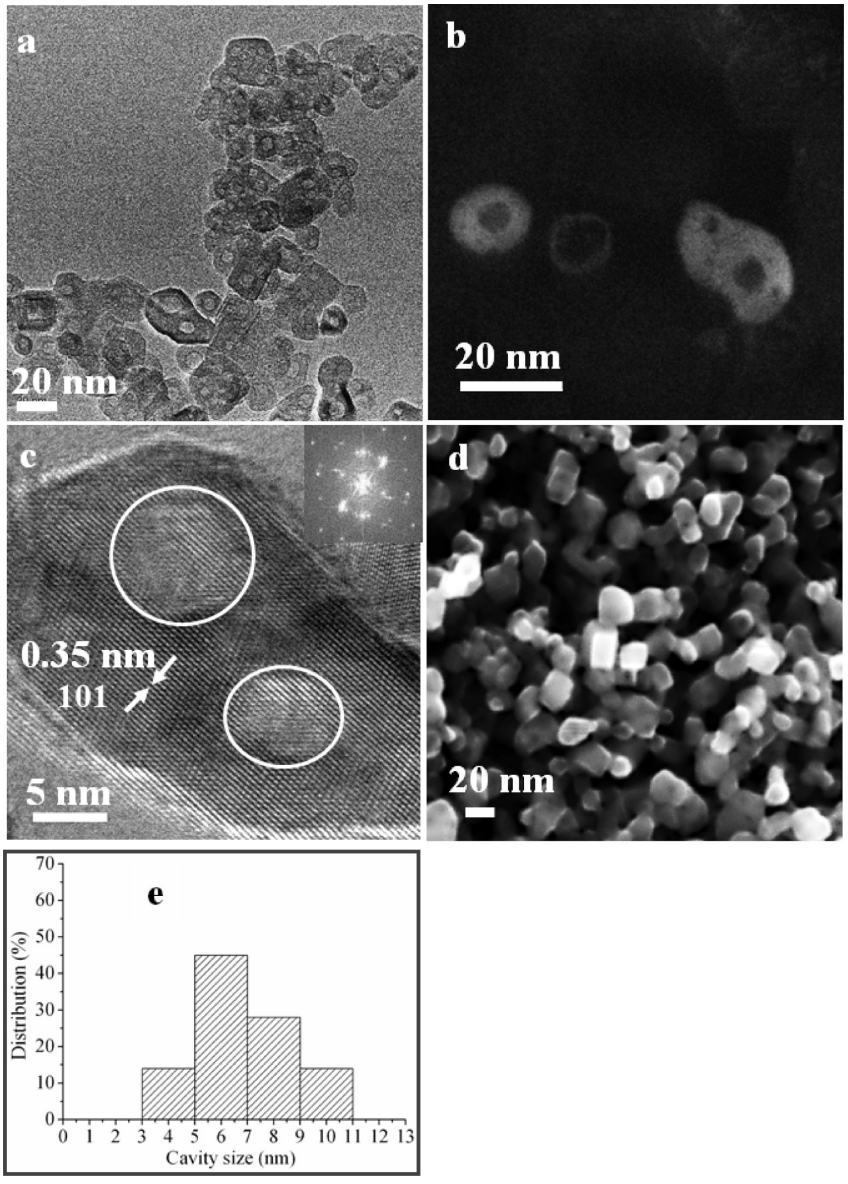

Figure 2. TEM (a), dark field TEM (b), HRTEM (c), and its corresponding FFT (inset of (c)). SEM image (d) of the TiO_2 nanocrystals with internal pores. Pore size distribution of the TiO_2 nanocrystals with internal pores (e).

hysteresis (Figure 3a), which is related to the capillary condensation associated with pores between the nanoparticles. BJH desorption pore size distribution (Figure 3b) of the TiO_2 nanocrystals with internal pores shows that there is almost no adsorption of N_2 for pores less than 7.0 nm, suggesting that the pores are buried and not accessible. The average pore size by its BJH desorption (19.2 nm) is much larger than the pore size by TEM, confirming that N_2 molecule could not diffuse into the pores of the TiO_2 nanocrystals with internal pores. Its BET surface area and total pore volume are 73.7 $m^2\ g^{-1}$ and 0.35 mL g^{-1}, respectively. The mesopores and their pore volume measured by BJH originate from the aggregation of the TiO_2 nanocrystals with internal pores (Figure 2d).

3.2. Formation Mechanism. *Role of HF.* To understand the formation mechanism of the TiO_2 nanocrystals with internal pores, microwave-assisted hydrolysis of $TiOCl_2$ in the

dx.doi.org/10.1021/am404457u | ACS Appl. Mater. Interfaces 2014, 6, 1608−1615

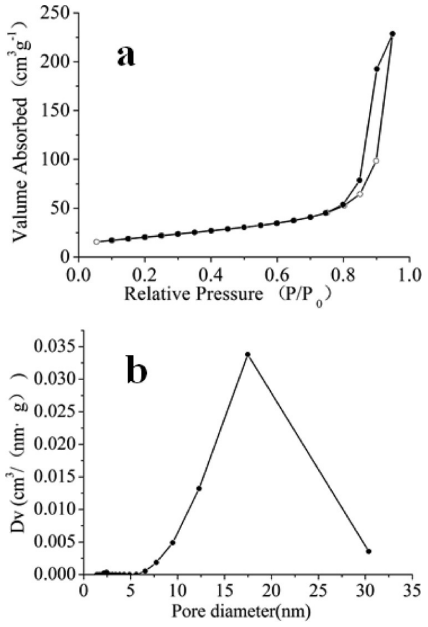

Figure 3. N_2 adsorption−desorption isotherm (a) and BJH desorption pore size distribution (b) of the TiO_2 nanocrystals with internal pores.

absence of HF followed by calcination at 400 °C was performed. In this case, TiO_2 solid nanoparticles without hollow structure are observed as shown in Figure 4a and b. XRD reveals that the TiO_2 solid nanoparticles are a mixture of anatase and rutile (Figure 1b, Table 1). The rutile content of the TiO_2 solid nanoparticles estimated by XRD is 43.0%.[33] The average crystal size of anatase and rutile estimated by XRD is 13.7 and 17.1 nm, respectively. This observation reveals that the presence of HF plays a crucial role in the formation of TiO_2 nanocrystals with internal pores and crystalline phase.

In the mixture of $TiOCl_2$ and HF aqueous solution, the exchange reaction between $TiCl_4$ and HF may take place:

$$TiOCl_2 + xHF = TiOCl_{2-x}F_x + xHCl$$

As the Ti−F bond is more stable than Ti−Cl bond due to its larger bonding energy (D_0 (Ti−F) = 569 kJ mol^{-1}) than that of Ti−Cl (D_0 (Ti−Cl) = 494 kJ mol^{-1}), the hydrolysis of Ti−Cl is faster than that of Ti−F in the process of the microwave-assisted hydrolysis of $TiOCl_{2-x}F_x$. Some unhydrolyzed Ti−F bonds exist in the formed TiO_2 nanoparticles. The including of fluorine in the formed TiO_2 nanoparticles is confirmed by energy dispersive spectral (EDS) analysis (Figure 5). With the evolution of hydrolysis and crystallization, pores are formed in the TiO_2 nanoparticles through fluoride-mediated surface dissolution.[34]

Role of Calcination. To elucidate the role of calcination in the formation of the TiO_2 nanocrystals with internal pores, we prepared TiO_2 sample by the microwave-assisted hydrolysis of a mixture of $TiOCl_2$ and HF aqueous solution with the same procedure as the TiO_2 nanocrystals with internal pores but without calcination at 400 °C. XRD results reveals that the uncalcined TiO_2 sample exhibits a pure anatase structure with an average crystal size of 11.8 nm (Figure 1c, Table 1). As can be seen from the TEM images of the uncalcined TiO_2 sample (Figure 4c), a number of pores exist in each TiO_2 nanoparticle with a size range of 4.3−28.6 nm. The size of the pores is 0.9−4.6 nm. The BET surface area of the uncalcined TiO_2 sample (190.8 m^2 g^{-1}) is much larger than that of the TiO_2 nanocrystals with internal pores. Remarkably, two high-index facets of {113} and {103} in addition to the most stable {101} facet are observed for the uncalcined TiO_2 sample (Figure 4d and e). The presence of the high-index facets suggests that the surface of the uncalcined TiO_2 sample is highly active owing to its unique surface atomic structures such as a high density of atomic steps, dangling bonds, kinks and ledges.[35] EDS analysis shows that the uncalcined TiO_2 sample contains 6.62 at% fluorine with F/Ti atomic ratio of 0.33. The uncalcined TiO_2 sample was also analyzed by XPS. Its content of fluorine and F/Ti atomic ratio by XPS is 7.12 atom % and 0.29, respectively, which are generally in agreement to those by EDS. These results indicate the presence of many Ti−F bonds which are not hydrolyzed in the process of the microwave-assisted hydrolysis and the following washing with distilled water. There is no detectable chlorine by both EDS and XPS for the uncalcined TiO_2 sample, further confirming that the Ti−F bond is more stable than Ti−Cl bond. The presence of Ti−F bonds can stabilize the high active facets by decreasing their surface energy.[36] Both the pore size (0.9−4.6 nm) and average crystal size (11.8 nm) of the uncalcined TiO_2 sample are smaller than those of the corresponding TiO_2 nanocrystals with internal pores calcined at 400 °C. These results suggest that the calcination at 400 °C leads to the coalition of small pores into large size pores accompanying with TiO_2 nanocrystal growth. EDS reveals that the calcination at 400 °C results in a decrease of the fluorine content from 6.62 to 3.01 atom % and a decrease of F/Ti atomic ratio from 0.33 to 0.095. XPS analysis indicates that after the calcination the fluorine content and F/Ti atomic ratio of the TiO_2 nanocrystals with internal pores decrease to 1.92 atom % and 0.086, respectively. The results suggest the removal of fluorine in the process of TiO_2 hollow nanocrystal formation.

Interestingly, after calcination at 400 °C, the high-index facets of {113} and {103} of the uncalcined TiO_2 sample disappear, and the resultant TiO_2 nanocrystals with internal pores only shows the most stable{101} facet, suggesting that the TiO_2 nanocrystal growth occurs at the expense of highly active high-index facets of {113} and {103}.

We further measured the distribution of the fluorine atoms in the TiO_2 nanocrystals with internal pores by XPS with Ar ion sputtering. Before Ar ion sputtering, the fluorine content and F/Ti atomic ratio of the TiO_2 nanocrystals with internal pores measured by XPS is 1.92 atom % and 0.086, respectively. After the Ar ion sputtering (3 kV, 2 μA for 300s), the fluorine content of the TiO_2 nanocrystals with internal pores decreases from 1.92 to 1.60 atom %, and its F/Ti atomic ratio decreases from 0.086 to 0.057. This result indicates that more fluorine atoms are located on the external surface rather than on the internal surface within the cavity of the TiO_2 nanocrystals with internal pores. This suggests that the growth of TiO_2 nanocrystals with internal pores occurs at the expense of the high-index facets of {113} and {103} accompanying with the removal of F atoms on the high-index facets of the uncalcined TiO_2 sample during the calcinations at 400 °C.

Effect of Calcination Temperature. We further increased the calcination temperature of the uncalcined TiO_2 sample from 400 to 600 °C. XRD analysis (Figure 1e) reveals that the obtained TiO_2 sample after calcination at 600 °C for 2 h still has a pure anatase structures. Its average crystal size determined by the Scherrer formula ($L = 0.89\lambda/\beta \cos\theta$) increases from 18.8 to 25.4 nm (Table 1, Sample e). In this case, although the TiO_2 nanocrystals with internal pores are clearly seen (Figure 6), the

dx.doi.org/10.1021/am404457u | ACS Appl. Mater. Interfaces 2014, 6, 1608−1615

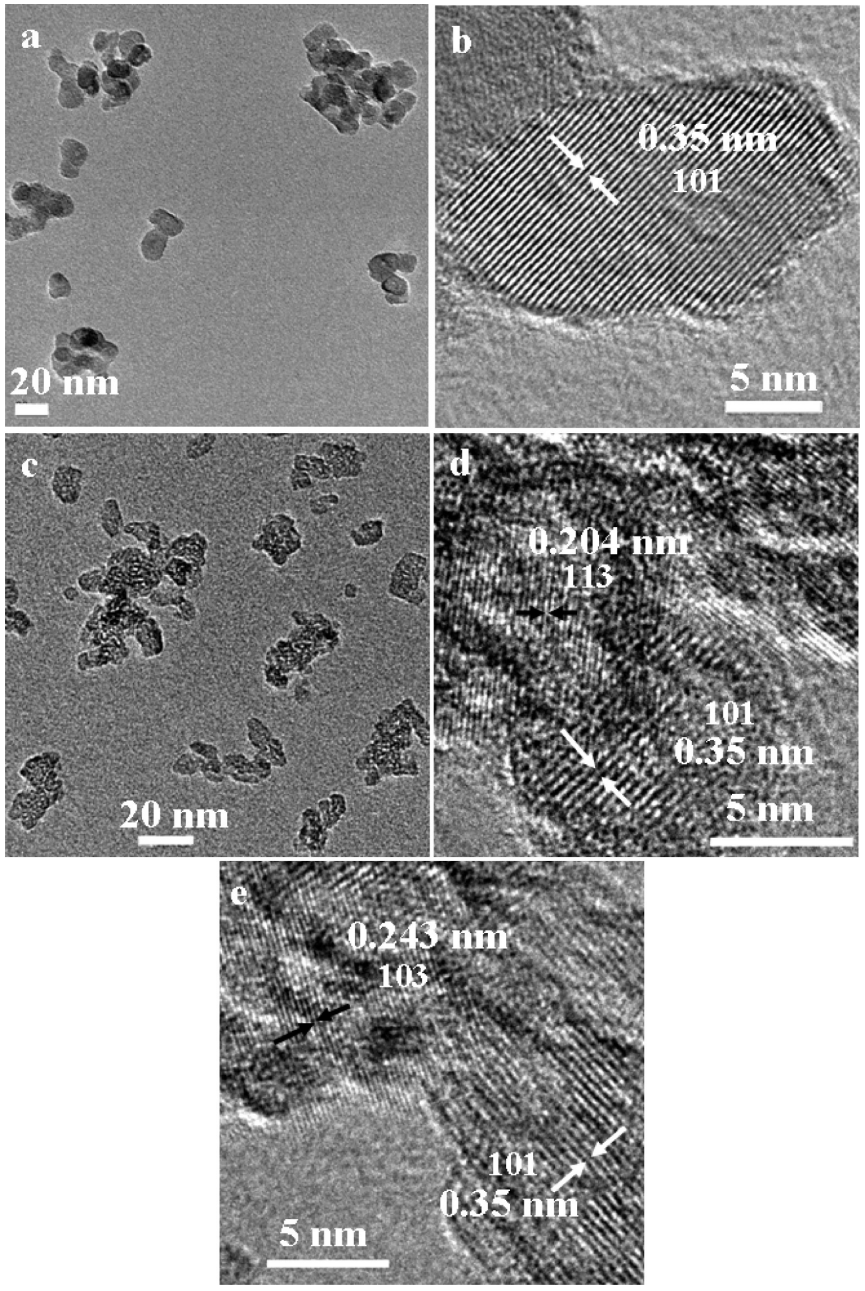

Figure 4. TEM and HRTEM images of the TiO_2 solid nanoparticles (a, b) and the uncalcined TiO_2 sample (c–e).

TiO_2 solid nanocrystals appears as shown in Figure 6a. XPS analysis indicates that the content of fluorine and F/Ti atomic ratio by XPS decreases to 0.42 atom % and 0.017, respectively. These results suggest that the internal pores in the TiO_2 nanocrystals collapses accompanying with the growth of TiO_2 nanocrystals.

3.3. Photocatalytic Activity. Dye effluents from textile industries are becoming a serious environmental problem because of their unacceptable color, high chemical oxygen demand content, and resistance to chemical, photochemical, and biological degradation. Photocatalysis in the presence of nanostructured TiO_2 provides an attractive approach to degrade spent dyes. Figure 7 shows the time course of the decrease in the concentration of crystal violet (CV) as cationic dye under the UV irradiation of a 125 W high-pressure Hg lamp. The TiO_2 nanocrystals with internal pores exhibit a higher photocatalytic activity than TiO_2 (P25), a widely used benchmark photocatalyst. After the UV irradiation for 80 min, 96.7% of CV is photodegraded on the TiO_2 nanocrystals with internal pores. In contrast, only 70.3% of CV is photodegraded on TiO_2(P25). To make comparison, we prepared pure anatase TiO_2 solid nanocrystals (Table 1, Supporting Information Figure S1) by a vapor induced hydrothermal hydrolysis at 180 °C using $Ti(OBu)_4$ as precursor, and measure its photocatalytic activity for CV photodegradation under the UV irradiation. As shown in Figure 7A, the TiO_2 solid nanocrystals exhibit much lower photocatalytic activity than the TiO_2 nanocrystals with internal pores. After the UV irradiation for 80 min, the photodegradation conversion on the solid TiO_2 nanocrystals is only 6.8%. The TiO_2 nanocrystals with internal pores contain 3.01 at% fluorine as discussed above. It has been reported that the fluorination of TiO_2 can considerably increase the

dx.doi.org/10.1021/am404457u | ACS Appl. Mater. Interfaces 2014, 6, 1608–1615

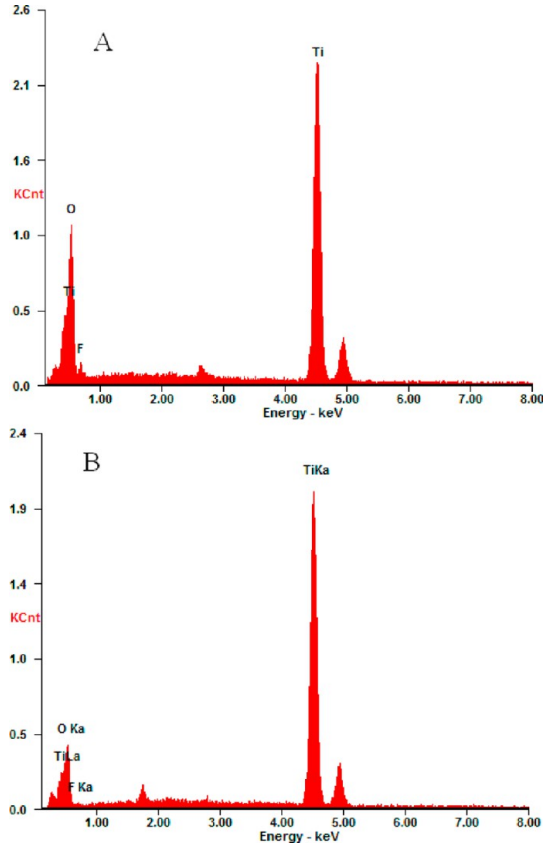

Figure 5. Energy dispersive spectra of the uncalcined TiO_2 sample with 6.62 at% F (A) and the TiO_2 hollow nanocrystal sample with 3.01 at% F (B).

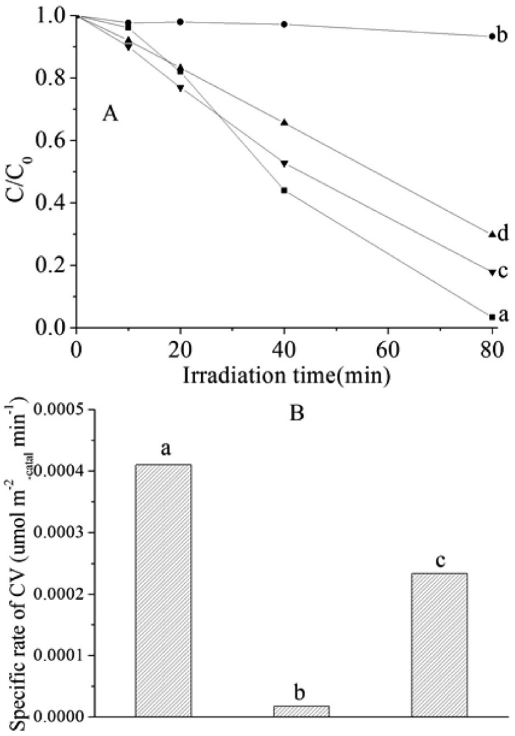

Figure 7. Time course of the decrease in the concentration of CV (A) and the specific rates of CV photodegradation (B) under the UV irradiation of a 125 W high-pressure Hg lamp: (a) TiO_2 nanocrystals with internal pores, (b) TiO_2 solid nanocrystals, (c) fluorinated TiO_2 solid nanocrystals, and (d)TiO_2(P25).

photocatalytic activity of TiO_2 photocatalysts,[37−40] because electron storage in the surface Ti−F moiety not only retards electron transfer to O_2, but also inhibits charge recombination that in turn significantly facilitates the interfacial hole transfer (to adsorbed H_2O or surface hydroxyl) to give rise to free OH radicals.[39,40] To elucidate whether the much higher photocatalytic activity of the TiO_2 nanocrystals with internal pores than the TiO_2 solid nanocrystals originates from the presence of fluorine in the TiO_2 nanocrystals with internal pores, we prepared a fluorinated TiO_2 solid nanocrystals with 3.01 atom % fluorine the same as the TiO_2 nanocrystals with internal pores by postsynthesis fluorination.[37] As shown in Figure 7A, the fluorination significantly increases the photocatalytic activity of the TiO_2 solid nanocrystals, which is in agreement to the reported results.[39] The fluorination of the TiO_2 solid nanocrystals lead to a considerable increase of the CV photodegradation conversion with the UV irradiation for 80 min from 6.8% to 82.2%. However, the fluorinated TiO_2 solid nanocrystals still exhibit a lower photocatalytic activity than the TiO_2 nanocrystals with internal pores.

We also tested the photodegradation of methyl orange (MO) as an anionic dye and 4-chlorophenol (4-CP) as a nonionic organic pollutant on the TiO_2 nanocrystals with internal pores and the fluorinated TiO_2 solid nanocrystals under the UV irradiation. Similarly, the TiO_2 nanocrystals with internal pores exhibit a higher photocatalytic activity than the fluorinated

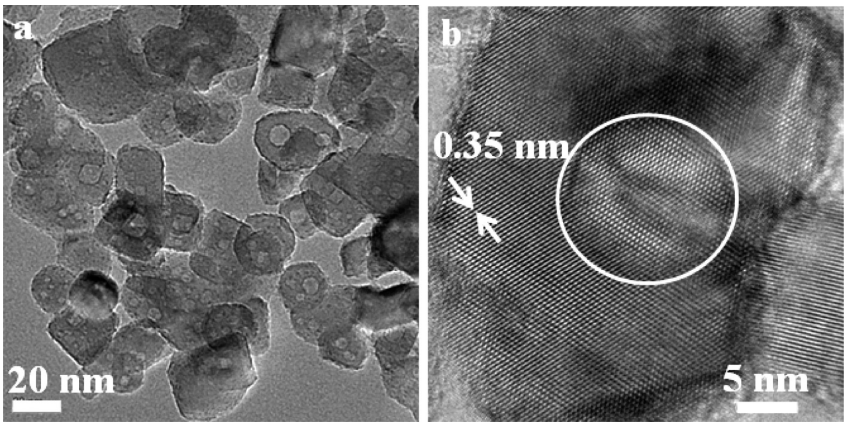

Figure 6. TEM (a) and HRTEM (b) images of the TiO_2 nanocrystals obtained by the calcination at 600 °C for 2 h of the uncalcined TiO_2 sample.

dx.doi.org/10.1021/am404457u | ACS Appl. Mater. Interfaces 2014, 6, 1608−1615

TiO_2 solid nanocrystals for the photodegradation of both MO and 4-CP (Figure 8).

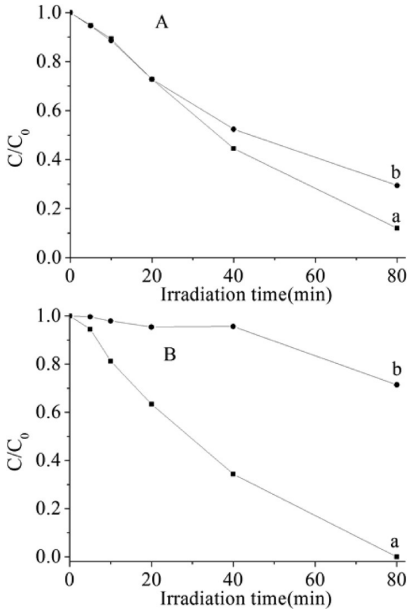

Figure 8. Time course of the decrease in the concentration of MO (A) and 4-CP (B) under the UV irradiation of a 125 W high-pressure Hg lamp: (a) TiO_2 nanocrystals with internal pores and (b) fluorinated TiO_2 solid nanocrystals.

As the TiO_2 catalysts have different specific surface areas, their specific rates of CV photodegradation (per unit surface area of catalyst), which represents the intrinsic photocatalytic efficiency of TiO_2, are compared. As shown in Figure 7B, the TiO_2 nanocrystals with internal pores exhibits the highest specific rates of CV photodegradation. Its specific rate (4.1×10^{-4} μmol m $^{-2}_{-catalyst}$ min^{-1}) is 23.3, 1.8 times higher than that of the TiO_2 solid nanocrystals and the fluorinated TiO_2 solid nanocrystals, respectively. These results suggest that the higher photocatalytic activity is due to the unique nanostructure of the TiO_2 nanocrystals with internal pores rather than the presence of fluorine and the difference of their specific surface area as compared with both the TiO_2 solid nanocrystals and the fluorinated TiO_2 solid nanocrystals.

3.4. Photocurrent. The widely accepted photoactivation mechanism is as follows: Upon UV excitation of TiO_2 by light absorption with energy equal to or greater than the band gap of the semiconductor, electrons are excited from the valence band to the conduction band. The photogenerated electrons (e) and holes (h) migrate from bulk to surface, where electrons reduce adsorbed electron acceptor (e.g., O_2) and holes oxidize adsorbed donor species (e.g., organic species or hydroxyl).[1,41] It is widely accepted that the e−h separation efficiency plays a decisive role in the photocatalytic reaction:[41] the higher the photocurrent is, the higher the e−h separation efficiency is, and thus the higher the photocatalytic activity is. Therefore, the photocurrent of the TiO_2 samples was measured under the UV irradiation. As shown in Figure 9, the TiO_2 nanocrystals with internal pores exhibit a higher photocurrent than the fluorinated TiO_2 solid nanocrystals, indicating that the e−h separation efficiency of the former is much higher than that of the latter.

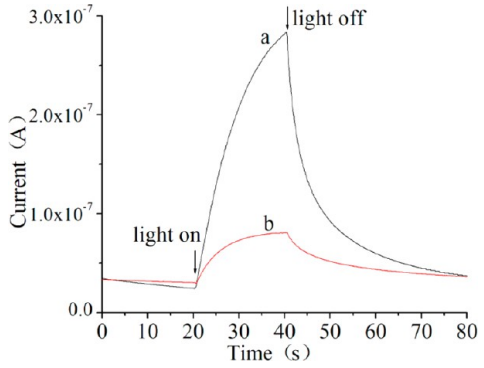

Figure 9. Transient response of the photocurrent for the TiO_2 samples under the UV irradiation in air: (a) the TiO_2 nanocrystals with internal pores and (b) the fluorinated TiO_2 solid nanocrystals.

The average crystal size of the TiO_2 nanocrystals with internal pores is 18.8 nm, and their pore dominant size is 5−7 nm as discussed above. Thus, the average wall thickness of TiO_2 nanocrystals with internal pores is 6.9−5.9 nm, which is smaller than the average crystal size of the TiO_2 solid nanocrystals (13.4 nm). Therefore, the higher e−h separation efficiency of the TiO_2 nanocrystals with internal pores than the fluorinated TiO_2 solid nanocrystals is most probably due to the thinner wall thickness of the TiO_2 nanocrystals with internal pores, which leads to the faster migration of the photoexcited electrons and holes from the internal to surface and better photocatalytic activity.

4. CONCLUSIONS

In summary, we develop a novel strategy conceptually different from the Kirkendall effect to prepare TiO_2 nanocrystals with internal pores by a facile microwave-assisted hydrolysis of $TiOCl_2$ aqueous solution in the presence of HF followed by calcination. The anatase TiO_2 nanocrystals with internal pores exhibit higher photocatalytic activity than the TiO_2 solid nanocrystals. This is attributed to the higher separation efficiency of photogenerated electrons and holes in the former than in the latter due to the unique nanostructure of the TiO_2 nanocrystals with internal pores. The TiO_2 nanocrystals with internal pores may have promising potential applications in environmental remediation, solar cell, renewable clean energy applications, and lithium ion batteries owing to the unique structure.

■ ASSOCIATED CONTENT

Supporting Information

TEM and HRTEM images of the anatase TiO_2 solid nanocrystals (Figure S1). This material is available free of charge via the Internet at http://pubs.acs.org.

■ AUTHOR INFORMATION

Corresponding Author

*E-mail: liyuanzhi66@hotmail.com.

Notes

The authors declare no competing financial interest.

■ ACKNOWLEDGMENTS

This work was supported by National Natural Science Foundation of China (21273169, 51032005), Research and Development Project of Hubei Province (2013BAA045), and

National Basic Research Program of China (2009CB939704). We thank Prof. J. Liu for his helpful discussion.

REFERENCES

(1) Chen, X. B.; Mao, S. S. *Chem. Rev.* **2007**, *107*, 2891−2995.
(2) Kong, L.; Lu, X.; Bian, X.; Zhang, W.; Wang, C. *J. Solid State Chem.* **2010**, *183*, 2421−2425.
(3) Ding, S.; Chen, J. S.; Wang, Z.; Cheah, Y. L.; Madhavi, S.; Hu, X.; Lou, X. W. *J. Mater. Chem.* **2011**, *21*, 1677−1680.
(4) Park, J. H.; Jung, S. Y.; Kim, R.; Park, N. G.; Kim, J.; Lee, S. S. *J. Power Sources* **2009**, *194*, 574−578.
(5) Kondo, Y.; Yoshikawa, H.; Awaga, K.; Murayama, M.; Mori, T.; Sunada, K.; Bandow, S.; Iijima, S. *Langmuir* **2008**, *24*, 547−550.
(6) Koo, H. J.; Kim, Y. J.; Lee, Y. H.; Lee, W. I.; Kim, K.; Park, N. G. *Adv. Mater.* **2008**, *20*, 195−199.
(7) Wang, H. Q.; Miyauchi, M.; Ishikawa, Y.; Pyatenko, A.; Koshizaki, N.; Li, Y.; Li, L.; Li, X. Y.; Bando, Y. S.; Golberg, D. *J. Am. Chem. Soc.* **2011**, *133*, 19102−19109.
(8) Liu, S.; Yu, J.; Jaroniec, M. *J. Am. Chem. Soc.* **2010**, *132*, 11914−11916.
(9) Xu, H.; Chen, X. Q.; Ouyang, S. X.; Kako, T.; Ye, J. H. *J. Phys. Chem. C* **2012**, *116*, 3833−3839.
(10) Truong, Q. D.; Le, T. S.; Hoa, H. T. *CrystEngComm* **2012**, *14*, 4274−4278.
(11) Jiang, P.; Bertone, J. F.; Colvin, V. L. *Science* **2001**, *291*, 453−457.
(12) Lou, X. W.; Archer, L. A. *Adv. Mater.* **2008**, *20*, 1853−1858.
(13) Wang, Z. Y.; Lou, X. W. *Adv. Mater.* **2012**, *24*, 4124−4129.
(14) Joo, J. B.; Zhang, Q.; Lee, I.; Dahl, M.; Zaera, F.; Yin, Y. D. *Adv. Funct. Mater.* **2012**, *22*, 166−174.
(15) Nakashima, T.; Kimizuka, N. *J. Am. Chem. Soc.* **2003**, *125*, 6386−6387.
(16) Li, X. X.; Xiong, Y. J.; Li, Z. Q.; Xie, Y. *Inorg. Chem.* **2006**, *45*, 3493−3495.
(17) Kim, Y. J.; Chai, S. Y.; Lee, W. *Langmuir* **2007**, *23*, 9567−9571.
(18) Li, J.; Zeng, H. C. *J. Am. Chem. Soc.* **2007**, *129*, 15839−15847.
(19) Li, H. X.; Bian, Z. F.; Zhu, J.; Zhang, D. Q.; Li, G. S.; Huo, Y. N.; Li, H.; Lu, Y. F. *J. Am. Chem. Soc.* **2007**, *129*, 8406−8407.
(20) Yu, J. G.; Guo, H. T.; Davis, S. A.; Mann, S. *Adv. Funct. Mater.* **2006**, *16*, 2035−2041.
(21) Pan, J.; Zhang, X.; Du, J.; Sun, D.; Leckie, J. O. *J. Am. Chem. Soc.* **2008**, *130*, 11256−11257.
(22) Zhou, J. K.; Lv, L.; Yu, J. Q.; Li, L.; Guo, P. Z.; Sun, H.; Zhao, X. S. *J. Phys. Chem. C* **2008**, *112*, 5316−5321.
(23) Shang, S. Q.; Jiao, X. L.; Chen, D. R. *ACS Appl. Mater. Interfaces* **2012**, *4*, 860−865.
(24) Li, D.; Qin, Q.; Duan, X. C.; Yang, J. Q.; Guo, W.; Zheng, W. J. *ACS Appl. Mater. Interfaces* **2013**, *5*, 9095−9100.
(25) Huang, Z.; Wang, Z. Y.; Lv, K. L.; Zheng, Y.; Deng, K. J. *ACS Appl. Mater. Interfaces* **2013**, *5*, 8663−8669.
(26) (a) Oveisi, H.; Rahighi, S.; Jiang, X. F.; Nemoto, Y.; Beitollahi, A.; Wakatsuki, S.; Yamauchi, Y. *Chem.—Asian J.* **2010**, *5*, 1978−1983. (b) Kimura, T.; Yamauchi, Y.; Miyamoto, N. *Chem.—Eur. J.* **2011**, *17*, 4005−4011. (c) Kimura, T.; Yamauchi, Y.; Miyamoto, N. *Chem.—Eur. J.* **2010**, *16*, 12069−12073.
(27) Yin, Y. D.; Rioux, R. M.; Erdonmez, C. K.; Hughes, S.; Somorjai, G. A.; Alivisatos, A. P. *Science* **2004**, *304*, 711−714.
(28) Henkes, A. E.; Vasquez, Y.; Schaak, R. E. *J. Am. Chem. Soc.* **2007**, *129*, 1896−1897.
(29) Peng, S.; Sun, S. H. *Angew. Chem., Int. Ed.* **2007**, *46*, 4155−4158.
(30) Fei, J. B.; Cui, Y.; Yan, X. H.; Qi, W.; Yang, Y.; Wang, K. W.; He, Q.; Li, J. B. *Adv. Mater.* **2008**, *20*, 452−456.
(31) Hung, L. I.; Tsung, C. K.; Huang, W. Y.; Yang, P. D. *Adv. Mater.* **2010**, *22*, 1910−1914.
(32) (a) Bass, J. D.; Grosso, D.; Boissiere, C.; Sanchez, C. *J. Am. Chem. Soc.* **2008**, *130*, 7882−7897. (b) Zhou, W.; Sun, F. F.; Pan, K.; Tian, G. H.; Jiang, B. J.; Ren, Z. Y.; Tian, C. G.; Fu, H. G. *Adv. Funct. Mater.* **2011**, *21*, 1922−1930.
(33) Li, Y. Z.; Fan, Y. N.; Chen, Y. *J. Mater. Chem.* **2002**, *12*, 1387−1390.
(34) Yu, J.; Xiang, Q.; Ran, J.; Mann, S. *CrystEngCommun* **2010**, *12*, 872−879.
(35) Jiang, H. B.; Cuan, Q.; Wen, C. Z.; Xing, J.; Wu, D.; Gong, X. Q.; Li, C. Z.; Yang, H. G. *Angew. Chem., Int. Ed.* **2011**, *50*, 3764−3768.
(36) Yang, H. G.; Sun, C. H.; Qiao, S. Z.; Zou, J.; Liu, G.; Smith, S. C.; Cheng, H. M.; Lu, G. Q. *Nature* **2008**, *453*, 638−641.
(37) Minero, C.; Mariella, G.; Maurino, V.; Pelizzetti, E. *Langmuir* **2000**, *16*, 2632−2641.
(38) Park, H.; Choi, W. *J. Phys. Chem. B* **2004**, *108*, 4086−4093.
(39) Yu, J. G.; Wang, W. G.; Cheng, B.; Su, B. L. *J. Phys. Chem. C* **2009**, *113*, 6743−6750.
(40) Liu, S. W.; Yu, J. G.; Cheng, B.; Jaroniec, M. *Adv. Colloid Interface Sci.* **2012**, *173*, 35−53.
(41) Thompson, L.; Yates, J. T., Jr. *Chem. Rev.* **2006**, *106*, 4428−4453.